Supplementary Information (SI) for Green Chemistry.
This journal is © The Royal Society of Chemistry 2026

Supporting information

Unlocking Vanadium Diboride As High-Performance Cathodes for Zinc-Ion Batteries

Yilei He [a,1], Lehuan Huang [a,1], Zining Li [a], Yang Li [a,b,*], Liubing Dong [a,*]

[a] College of Chemistry and Materials Science, Jinan University, Guangzhou 511443, China

[b] School of Materials and Energy, Foshan University, Foshan 528000, China

* Corresponding author. *Email address*: donglb@jnu.edu.cn

[1] These two authors contributed equally to this work.

1. Experimental section

1.1 Synthesis of VB_2 and EA-VB_2 cathode

The VB_2 cathode was obtained by mixing 12.56 mg of VB_2 powder and 157 mg of CNT aqueous slurry (Model: NTP2021; Shenzhen Nanotech Port Co., Ltd. The multi-walled CNTs were produced by chemical vapour deposition method, and they possess a length of 5~15 μm and diameter of 15~25 nm) in 100 ml of deionized water and then ultrasonically mixing for 10 min to form a homogeneous suspension. The VB_2 electrode was prepared by vacuum filtration of the VB_2-CNT slurry, which did not contain any collector, binder, or conductive additives. Subsequently, the electrode was dried under vacuum conditions for 12 h until it was ready for use. The mass loading of VB_2 in the electrode was 1.0 mg/cm^2. To enhance the electrochemical performance of VB_2 cathodes, the cathodes underwent an electrochemical activation treatment as follows: they were charged to 1.8 V at a high current density of 5 A/g and maintained at this voltage for 3 h. After the charging process, EA-VB_2 electrodes with higher electrochemical activity were obtained. By varying the charging voltage and constant voltage duration, VB_2 cathodes with different electrochemical performances can be achieved.

1.2 Materials characterization

The micro-morphology of materials was observed by scanning electron microscopy (SEM, model: Sigma 300) and high-resolution transmission electron microscopy (HRTEM, model: FEI Tecnai G2 F20). X-ray diffraction (XRD) patterns were obtained on an X-ray diffractometer (Miniflex 600) using Cu Kα (λ=1.5406 Å) as the source of radiation. The elemental composition of the sample surface was analyzed by X-ray photoelectron

spectroscopy (XPS, model: Thermo Scientific K-Alpha), and Laser Raman spectroscopy (model: Lab RAM HRE volution equipped with 532 nm laser excitation).

1.3 Electrochemical measurement

The EA-VB_2 cathode can be directly used as binder-free working electrodes for rechargeable aqueous zinc-based batteries. CR2032 coin cells were assembled by using the EA-VB_2 cathode, Zn foil anode, glass fiber separator, and 2 M $ZnSO_4$ aqueous electrolyte. Cyclic voltammetry (CV) was recorded on a Bio-Logic VSP-300 electrochemical workstation. The relationship between the scan rate v and the redox peak current can be described by the following equation,

$$i=av^b \tag{S1}$$

the b-value is a constant ranging from 0.5 to 1.0, where capacitive-controlled processes are characterized by b = 1.0, while diffusion-controlled processes are characterized by b = 0.5. Based on these b-values, the relative contributions of diffusion and capacitive processes can be quantified using the equations,

$$i=k_1v+k_2v^{1/2} \tag{S2}$$

where represents the capacitive contribution and represents the diffusion-controlled faradaic insertion contribution. The galvanostatic charge-discharge (GCD) tests, cycling tests, galvanostatic intermittent titration technique (GITT) were also performed on a LAND CT2001A battery-testing system. During the GITT measurements, a current of 0.5 A/g was adopted for 10 min and a pulse of 30 min was applied to collect the potential response. The energy density was directly calculated by integrating the GCD profiles, as expressed using the following formula:

$$E=\int C\times U \tag{S3}$$

where E is the energy density (Wh/kg), C is the specific capacity (mAh/g) and U is the voltage (V) in the GCD profiles. Note that the energy density was calculated based on the activate material mass of the cathodes, as widely did in the field of ZIBs, considering the excessive mass of the zinc anodes. The zinc-ion diffusion coefficient ($D_{Zn^{2+}}$) was calculated based on:

$$D_{Zn^{2+}}=\frac{4L^2}{\pi\tau}\left(\frac{\Delta E_s}{\Delta E_\tau}\right)^2 \tag{S4}$$

where the L, τ, ΔE_s, and ΔE_τ correspond to the thickness of the cathode (cm), the relaxation time (s), the steady state voltage (V) and voltage change (V) during the charge-discharge

process, respectively. CV and electrochemical impedance spectroscopy (EIS) tests were recorded on a Bio-Logic VSP-300 electrochemical workstation, with a frequency range of 0.1-100.0 kHz by applying a disturbance amplitude of 5 mV.

1.4 Computational methods

In order to study the diffusion of Zn-ion in crystalline VB_2, we have performed density functional theory (DFT) calculations using the Vienna *ab* initio Simulation Package (VASP).[S1,S2] The projector augmented wave (PAW) method and Perdew-Burke-Ernzerhof (PBE) functional were used throughout the work.[S3,S4] The kinetic cutoff energy was 500 eV and GAMMA-centered *k*-point mesh to 9×9×9 for the geometric relaxation and electronic structure calculations. Structural optimization of ground states was performed by allowing the lattice parameters and atomic positions to relax until the maximum force on each atom was less than 0.01 eV/Å. To investigate the zinc-ion occupation and migration behaviors, the binding energy of zinc-ions at the interstitial site within the VB_2 lattice was systematically calculated. The energy was obtained by evaluating the total energy differences between configurations with and without zinc intercalation at specific positions. The simulation box contains a 3×3×4 supercell with 108 atoms in total. The climbing-image nudged-elastic-band (CI-NEB) method was employed to search for minimum energy paths (MEP).[S5,S6] In the CI-NEB calculations, the mesh is 3×3×3, five images were utilized, and the atomic force was set to 0.05 eV/Å.

2. Supporting Figures and Tables

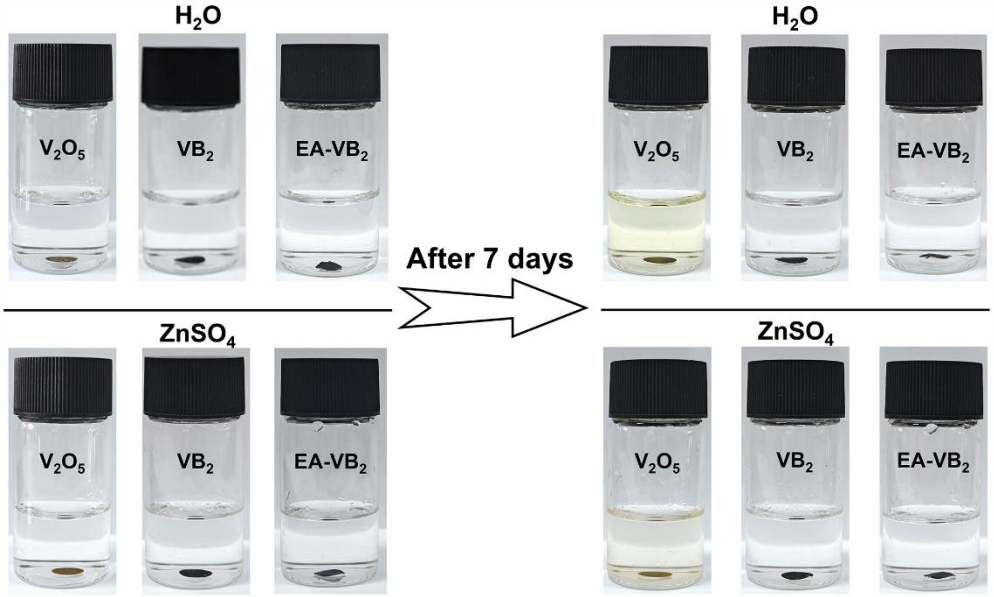

Figure S1. Spontaneous dissolution tendency tests of the V_2O_5, VB_2 and EA-VB_2 cathodes in water and 2 M $ZnSO_4$ electrolyte. For the V_2O_5 cathode, the vanadium dissolution issue is clearly observed since the solutions turn from transparent to yellow. In contrast, the VB_2 and EA-VB_2 cathode materials do not show obvious vanadium dissolution, as reflected by the almost unchanged color of the solutions after the cathodes were soaked for 7 days.

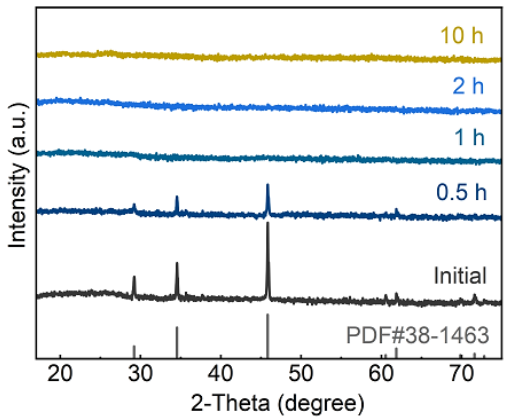

Figure S2. XRD patterns of the EA-VB_2 material obtained by electrochemically activating the pristine VB_2 at a constant voltage of 1.8 V for different activation times.

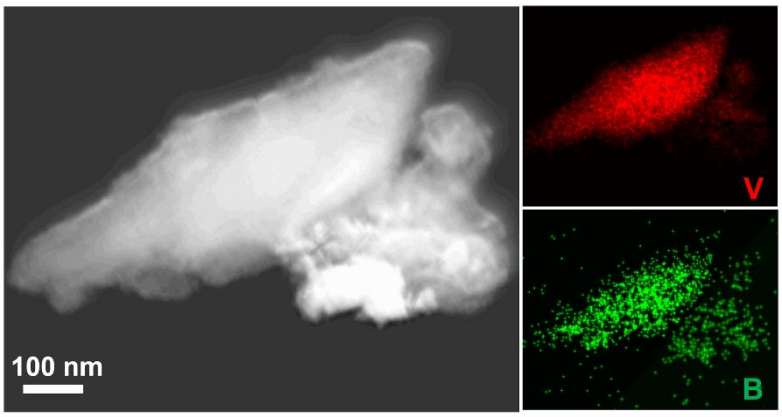

Figure S3. TEM-EDS elemental mapping images of the pristine VB_2 material.

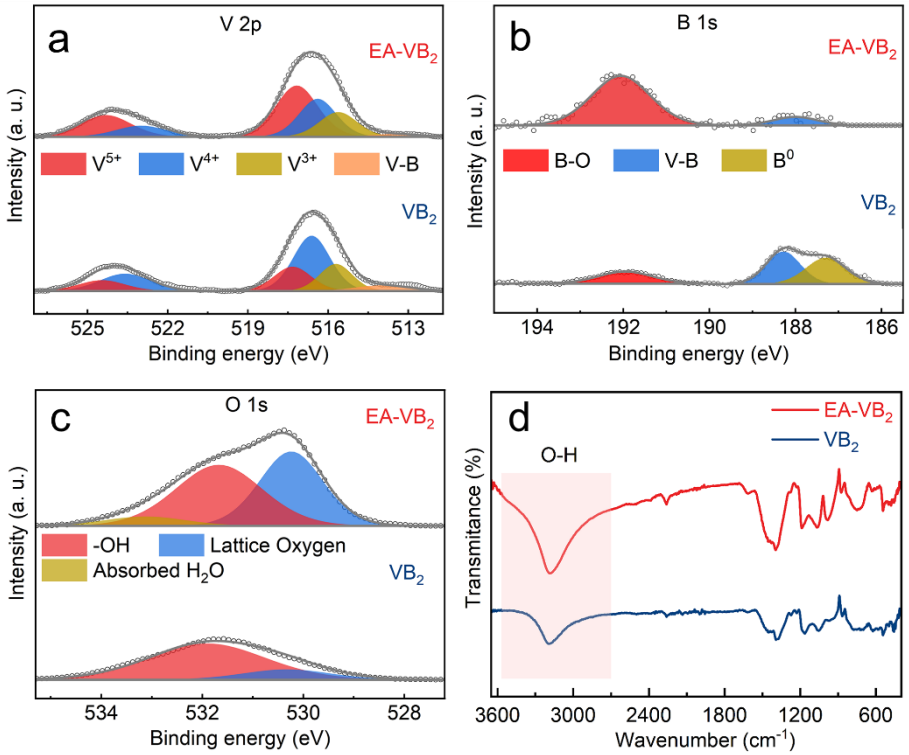

Figure S4. High-resolution XPS spectra of (a) V 2p, (b) B 1s, (c) O 1s and (d) FTIR spectra of the VB_2 and EA-VB_2 cathodes.

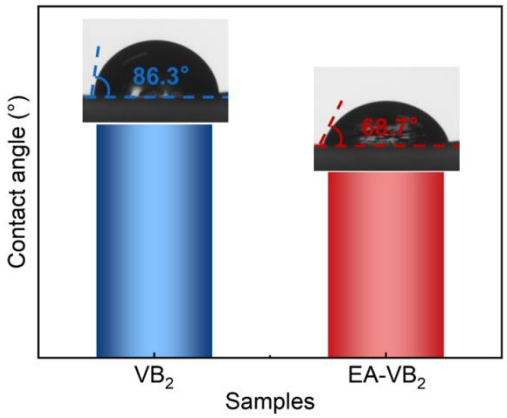

Figure S5. Contact angles of the VB_2 and EA-VB_2 cathodes.

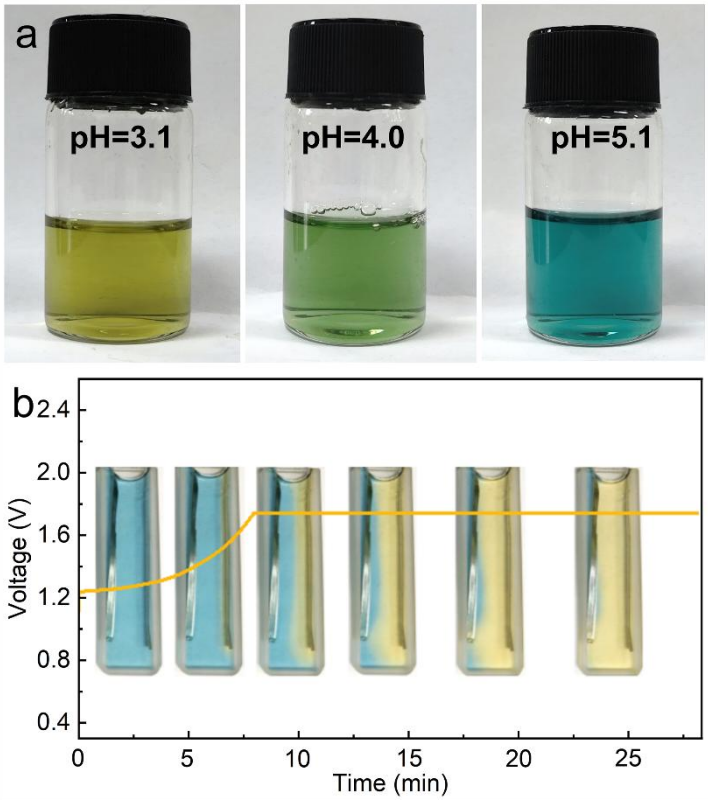

Figure S6. (a) The color of bromocresol green-containing 2 M $ZnSO_4$ electrolytes at different pH values. The initial pH of the 2 M $ZnSO_4$ electrolyte is 4.0, while the electrolytes with pH values of 3.1 and 5.1 were obtained by adding HCl or NaOH, respectively. The volume fraction of bromocresol green in the 2 M $ZnSO_4$ electrolyte is 0.6%. (b) pH variation of the electrolyte near the VB_2 cathode during the electrochemical activation process (the left and the right electrodes are zinc anode and the VB_2 cathode, respectively).

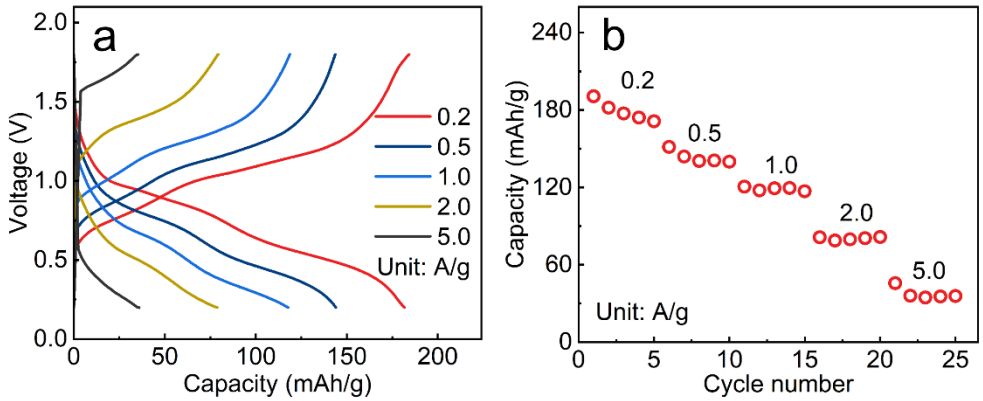

Figure S7. (a) GCD profiles and (b) rate performance of the EA-VB_2 cathodes (electrochemically activated in 0.1 M $Zn(CF_3SO_3)_2$/acetonitrile organic electrolyte). The electrochemical performance tests were performed in 2 M $ZnSO_4$ aqueous electrolyte.

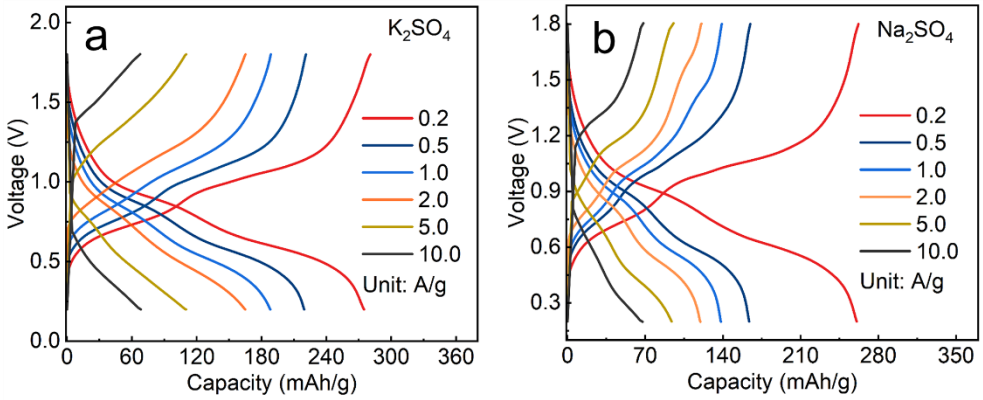

Figure S8. GCD profiles of the VB_2 cathodes after electrochemical activation in different electrolytes: (a) 0.5 M K_2SO_4; (b) 2 M Na_2SO_4. Note that the electrochemical activation was performed in the system with the pristine VB_2 cathode, activated carbon fiber (ACF) anode and the K_2SO_4 (or Na_2SO_4) electrolyte. After the activation process, the cathode was assembled into ZIBs with 2 M $ZnSO_4$ electrolyte for the above electrochemical tests.

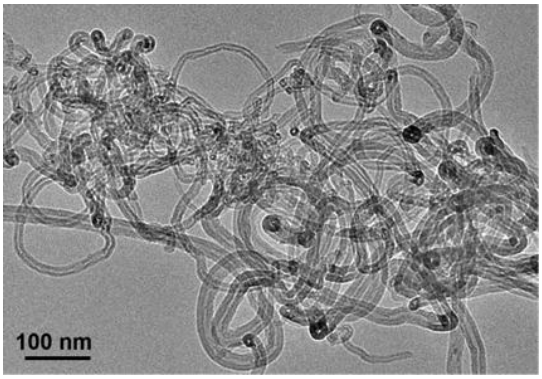

Figure S9. TEM image of the CNT raw-material.

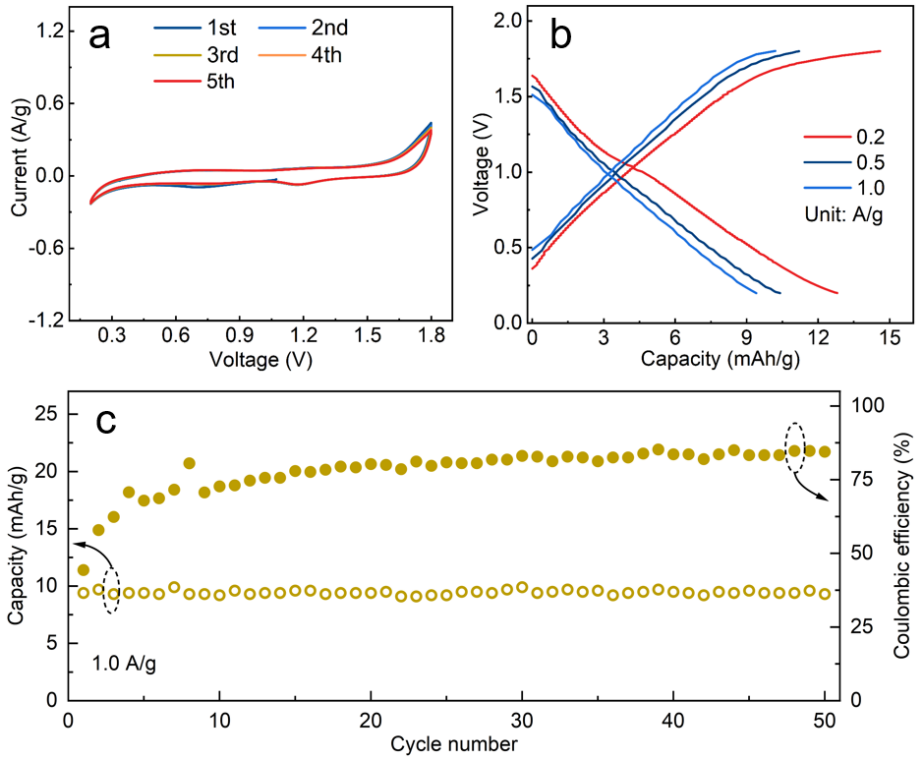

Figure S10. (a) CV curves at 1 mV/s, (b) GCD profiles and (c) cycling performance of the CNT cathode.

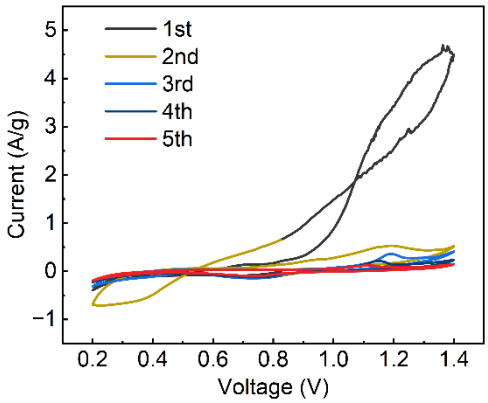

Figure S11. CV curves of the pristine VB_2 cathode at 1 mV/s.

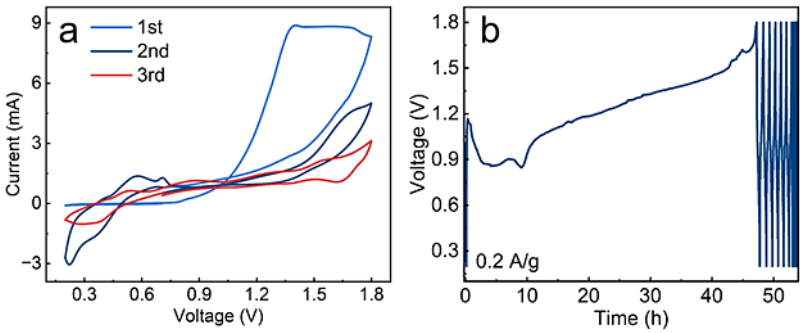

Figure S12. The electrochemical behavior of the pristine VB_2 cathode within the working voltage window of 0.2-1.8 V: (a) CV curves at 1 mV/s and (b) GCD profiles at 0.2 A/g. The CV curves present poor reversibility of the pristine VB_2 within 0.2-1.8 V, as consistent with the serious side reaction at the first charge process during the GCD tests, negatively affecting the cycling performance of the ZIBs. Even after the first charge/discharge cycle, its capacity (91 mAh/g at 0.2 A/g) is much inferior to the EA-VB_2 cathode synthesized by electrochemical activation.

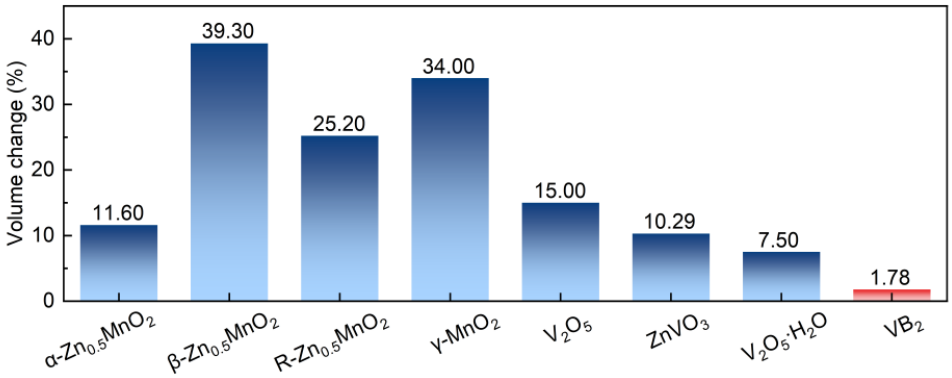

Figure S13. Zn^{2+} insertion-caused volume change comparison between the VB_2 and various reported cathode materials.[S7-S10]

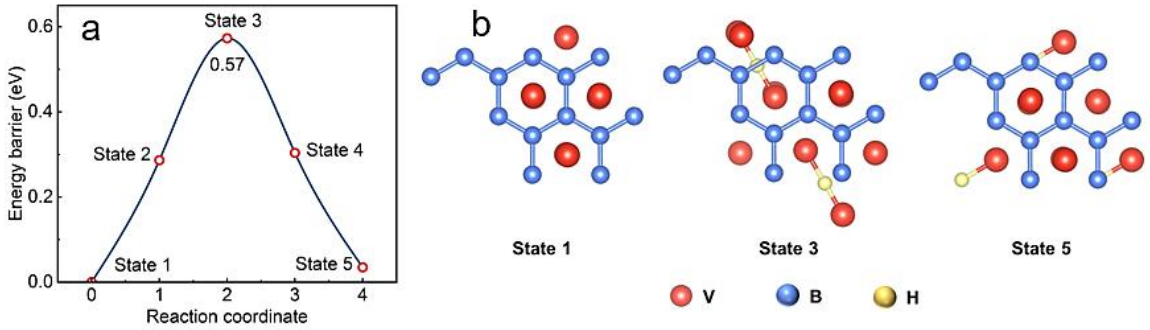

Figure S14. (a) Energy barriers and (b) corresponding crystal structures for the H^+ diffusion in the VB_2 cathode.

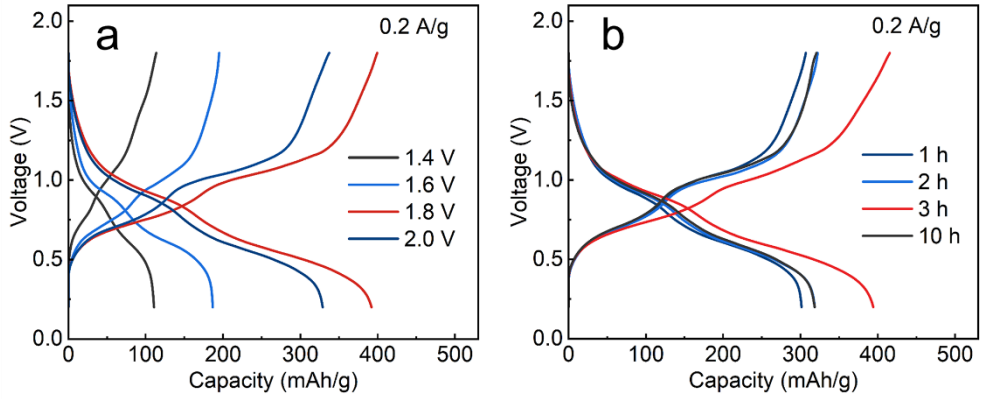

Figure S15. (a) GCD profiles of the EA-VB_2 cathodes synthesized under various electrochemical activation conditions: (a) different activation voltages from 1.4 to 2.0 V (activation time is 3 h); (b) different activation times from 1 to 10 h (activation voltage is 1.8 V).

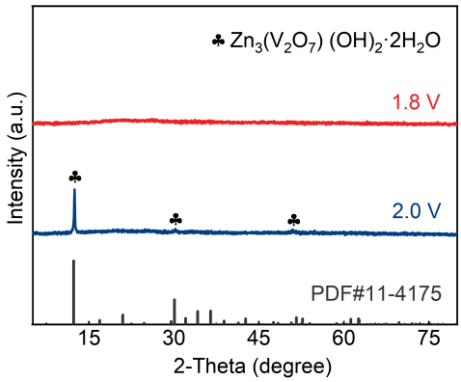

Figure S16. XRD patterns of the EA-VB_2 cathode synthesized under the electrochemical activation voltage of 1.8 and 2.0 V. Once the electrochemical activation voltage reaches 2.0 V, a new V-based oxide, zinc pyrovanadate ($Zn_3(V_2O_7)(OH)_2 \cdot 2H_2O$, PDF#11-4175), forms on the EA-VB_2 cathode. As pointed out in the previous research,[S11,S12] the Zn^{2+}-storage capacity of zinc pyrovanadate is lower than 150 mAh/g.

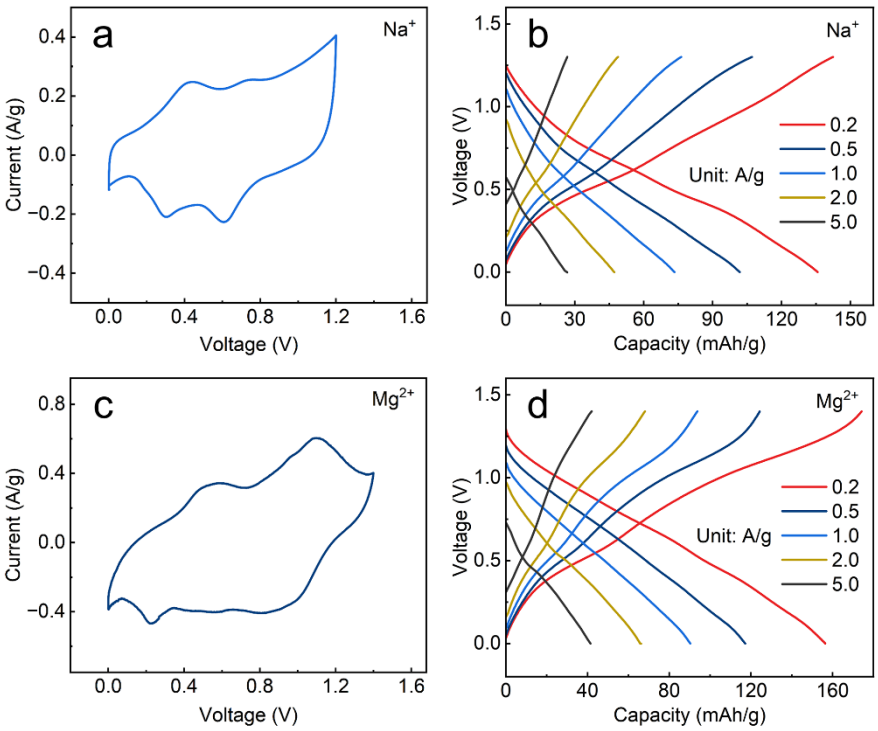

Figure S17. The CV curves at 1 mV/s and GCD profiles of the hybrid capacitors with the EA-VB_2 cathode and the ACF anode in (a-b) 2 M Na_2SO_4 and (c-d) 2 M $MgSO_4$ aqueous electrolytes.

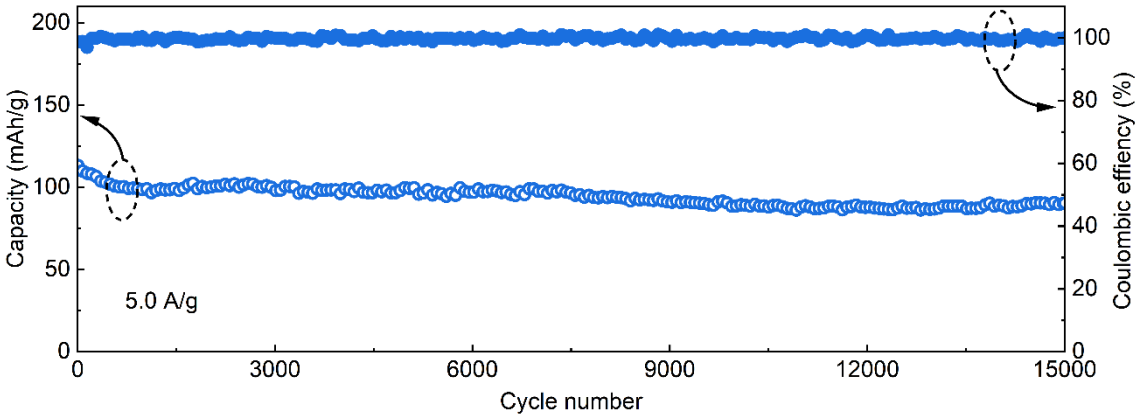

Figure S18. Cycling stability of the EA-VB_2 cathode-based zinc-ion hybrid supercapacitors.

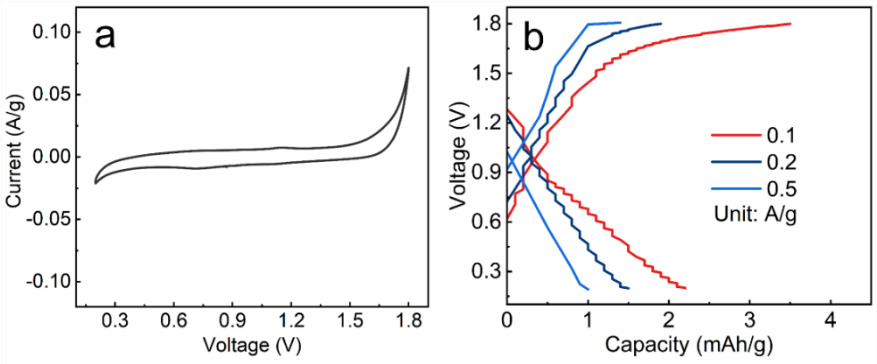

Figure S19. (a) CV curve at 1 mV/s and (b) GCD profiles at various current densities of B_2O_3 cathode in 2 M $ZnSO_4$ aqueous electrolyte. B_2O_3 shows poor electrochemical activity.

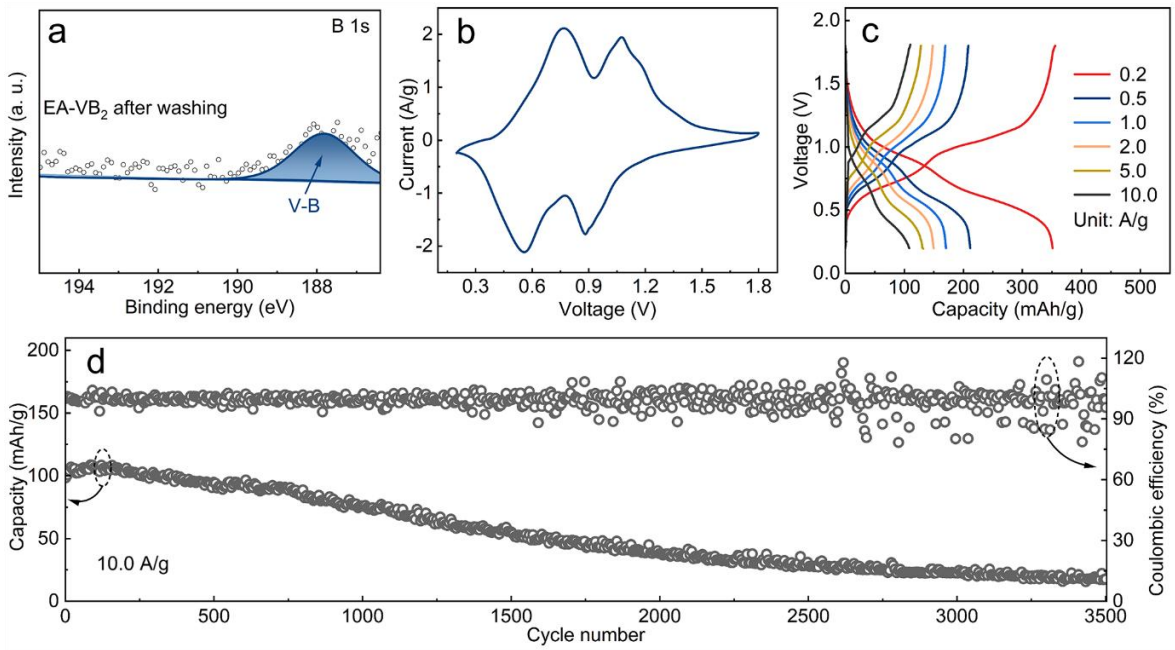

Figure S20. (a) B 1s XPS spectrum, (b) CV curve at 1 mV/s, (c) GCD profiles and (d) cycling performance of the EA-VB_2 cathode after washing with ethanol to remove the B_2O_3 component. From the XPS analysis, the characteristic peaks of B^{3+} disappear, proving that B_2O_3 has been successfully washed away because boron oxides are readily soluble in ethanol. The operating voltage window, redox peaks, and capacity at various current densities change slightly before and after the removal of the B_2O_3 component from the EA-VB_2 cathode, indirectly demonstrating that the B_2O_3 component does not participate in the ion-storage redox reactions. However, the cycling performance deteriorates significantly once the B_2O_3 component is removed, which illustrates the positive role of the B_2O_3 in stabilizing the structure of the EA-VB_2 cathode.

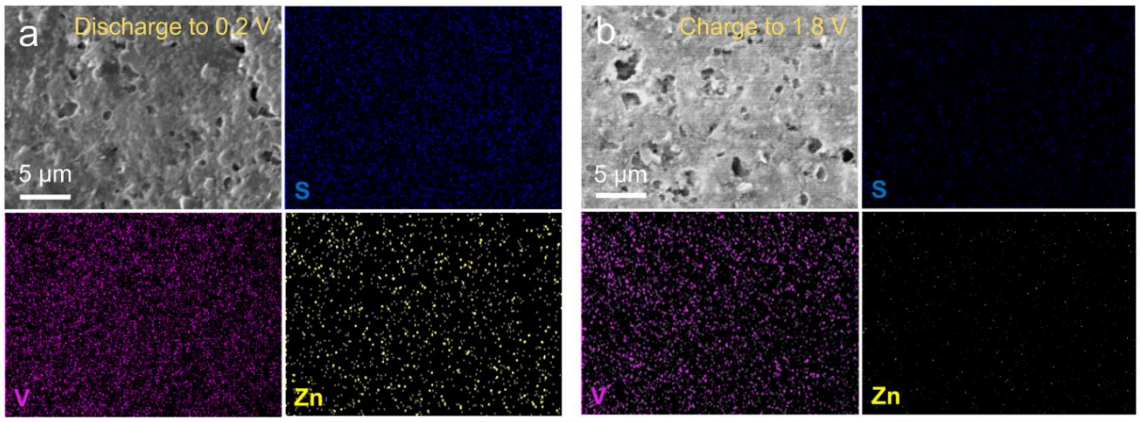

Figure S21. SEM-EDS elemental mapping images of the EA-VB_2 cathode at (a) fully discharged and (b) charged states. The cathodes were washed with 0.1 M HCl aqueous solution to eliminate the interference from $Zn_4SO_4(OH)_6{\cdot}5H_2O$ by-product before the SEM-EDS

analysis.

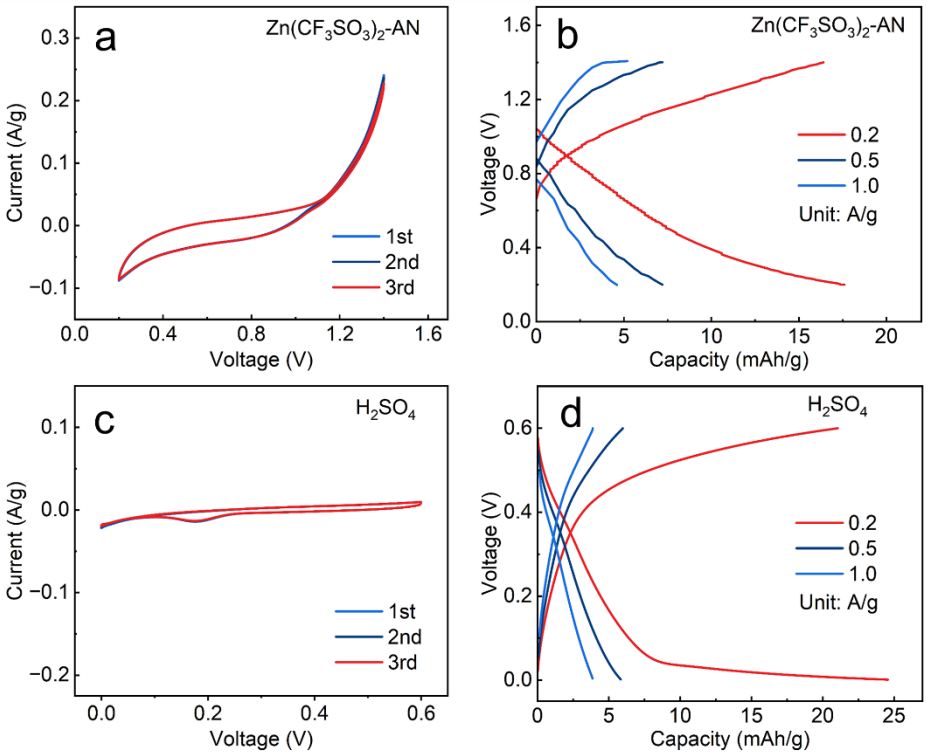

Figure S22. (a) CV curves at 1 mV/s and (b) GCD profiles of the VB_2 cathode in H^+-free $Zn(CF_3SO_3)_2$/AN electrolyte. (c) CV curves at 1 mV/s and (d) GCD profiles of the VB_2 cathode in Zn^{2+}-free H_2SO_4 aqueous electrolyte.

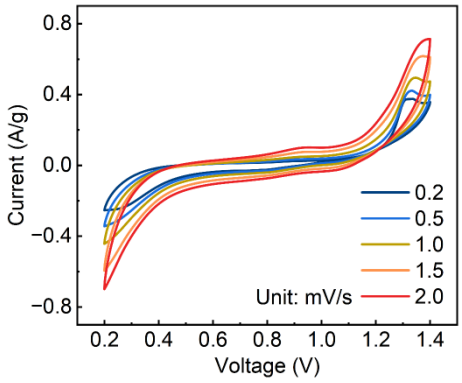

Figure S23. CV curves of the VB_2. cathode.

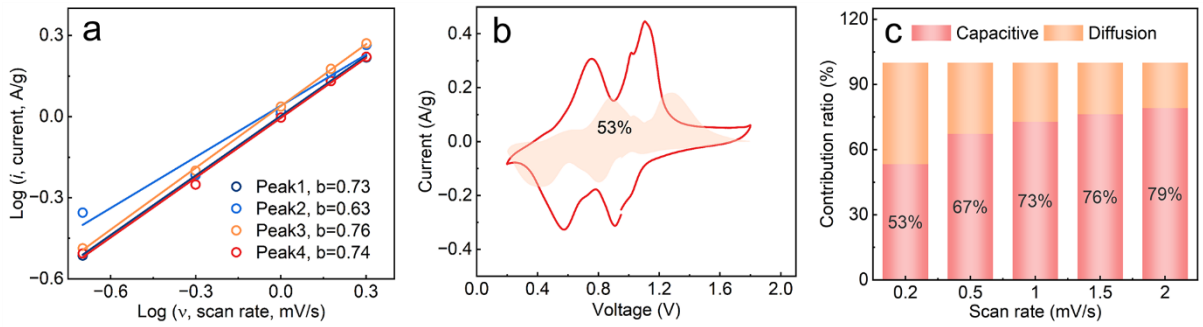

Figure S24. (a) Log (*i*) versus log (*v*) plots, (b) CV curves with capacitive contribution at 0.2 mV/s, and (c) capacitive contribution ratios at various sweep rates for the EA-VB_2 cathode.

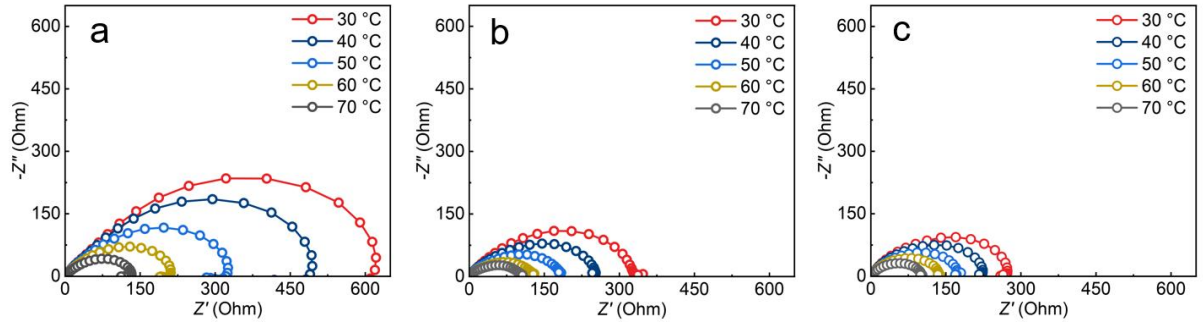

Figure S25. EIS spectra measured at various temperatures of the Zn//Zn symmetric cells using different separators: (a) CNF separator, (b) CNF@VB_2 separator and (c) CNF@EA-VB_2 separator.

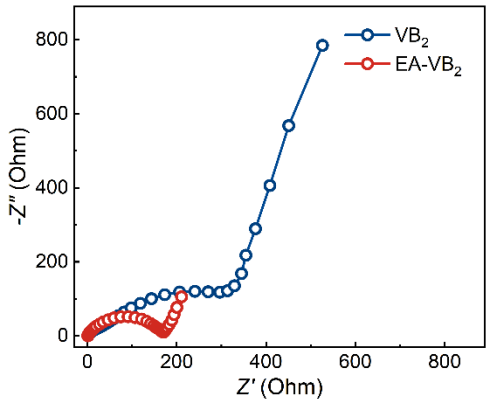

Figure S26. EIS spectra of the VB_2 and EA-VB_2 cathodes.

Table S1. Comparison of the electrochemical performance for the EA-VB_2 and some representative cathodes in ZIBs

Cathode	Electrolyte	Voltage windows (V)	Specific capacity (mAh/g)	Cycle performance	*Ref.*
EA-VB_2	2 M $ZnSO_4$	0.2-1.8	398.0 (0.2 A/g)	99.0% after 3500 cycles (10.0 A/g)	This work
TPA-V_{10}	3 M $Zn(CF_3SO_3)_2$	0.2-1.8	324.9 (0.1 A/g)	98.6% after 600 cycles (2.0 A/g)	[S13]
2D MnO/C	3 M $ZnSO_4$ + 0.1 M $MnSO_4$	0.8-1.8	210.0 (0.1 A/g)	90.0% after 900 cycles (0.5 A/g)	[S14]
HCN@MoS_2	3 M $Zn(OTf)_2$	0.6-1.6	328.0 (1.0 A/g)	83.6% after 4000 cycles (0.1 A/g)	[S15]
RuO_2 QDs@PCNCs	2 M $ZnSO_4$	0.4-1.8	224.0(0.2 A/g)	69.4% after 2000 cycles (1.0 A/g)	[S16]
A-VOP/G	1 M $Zn(CF_3SO_3)_2$ + 21 M $LiN(CF_3SO_2)_2$	0.8-2.1	168.4 (0.1 A/g)	87.7% after 1000 cycles (1.0 A/g)	[S17]
$VS_2/Ti_3C_2T_z$	1 M $ZnSO_4$	0.0-1.3	285.0 (0.2 A/g)	74.3% after 5000 cycles (2.0 A/g)	[S18]
Cu-$Bi_{2-x}Se_3$	1 M $ZnSO_4$	0.2-1.6	320.0 (0.1 A/g)	71.6% after 4000 cycles (10.0 A/g)	[S19]
VS-450	2 M $ZnSO_4$	0.4-1.5	370.0 (0.1 A/g)	83.6% after 1000 cycles (0.1 A/g)	[S20]
Cu-TBPQ MOF	3 M $Zn(CF_3SO_3)_2$	0.2-1.5	209.3 (0.1 A/g)	88.0% after 5000 cycles (2.0 A/g)	[S21]
PMVO-sls	2.8 M $Zn(CF_3SO_3)_2$ + 0.2 M $ZnSO_4$	0.2-1.8	329.0 (0.2 A/g)	85.0% after 100 cycles (0.2 A/g)	[S22]
DOP	2 M $Zn(ClO_4)_2$	0.3-1.5	336.0 (0.1 A/g)	85.0% after 2000 cycles (1.0 A/g)	[S23]
p-CD	2.5 M $Zn(CF_3SO_3)_2$	0.2-1.6	237.0 (0.1 A/g)	90.8% after 1000 cycles (1.0 A/g)	[S24]
lle-α-MnO_2	2 M $ZnSO_4$ + 0.2 M $MnSO_4$	0.8-1.8	332.8 (0.1 A/g)	85.0% after 2000 cycles (1.0 A/g)	[S25]
V_d-NVO	2 M $ZnSO_4$	0.4-1.5	371.0 (0.1 A/g)	81.7% after 1000 cycles (5.0 A/g)	[S26]

MoS_2/MWCNTs	2 M $ZnSO_4$	0.2-1.0	216.1 (0.1 A/g)	74.0% after 1000 cycles (3.0 A/g)	[S27]
δ-MnO_2	2 M $ZnSO_4$+ 0.2 M $MnSO_4$	0.8-1.8	308.0 (0.1 A/g)	66.7% after 600 cycles (1.0 A/g)	[S28]

References

[S1] G. Kresse, J. Furthmüller, *Comp. Mater. Sci.* 1996, **6**, 15.

[S2] G. Kresse, J. Furthmüller, *Phys. Rev. B* 1996, **54**, 11169.

[S3] J. Perdew, K. Burke, M. Ernzerhof, *Phys. Rev. Lett.* 1996, **77**, 3865.

[S4] G. Kresse, D. Joubert, *Phys. Rev. B* 1999, **59**, 1758.

[S5] G. Henkelman, B. Uberuaga, H. Jónsson, *J. Chem. Phys.* 2000, **113**, 9901.

[S6] D. Sheppard, P. Xiao, W. Chemelewski, D. Johnson, G. Henkelman, *J. Chem. Phys.* 2012, **136**, 074103.

[S7] T. Li, N. Zhang, B. Liu, P. Wang, Z. Liu, Y. Wang, D. Xu, H. Tian, Q. Zhang, T. Yi, *Adv. Funct. Mater.* 2025, **35**, 2423755.

[S8] T. Juran, J. Young, M. Smeu, *J. Phys. Chem. C* 2018, **122**, 8788.

[S9] T. Wu, K. Zhu, C. Qin, K. Huang, *J. Mater. Chem. A* 2019, **7**, 5612.

[S10] H. Zhang, F. Ning, Y. Guo, S. Subhan, X. Liu, S. Shi, S. Lu, Y. Xia, J. Yi, *ACS Energy Lett.* 2024, **9**, 4761.

[S11] C Xia, J Guo, Y Lei, H Liang, C Zhao, H Alshareef, *Adv. Mater.* 2018, **30**, 1705580.

[S12] C. Yuan, H. Liu, L. Liu, S. Fan, Z. Chen, H. Wang, W. Peng, Y. Li, Q. Zhang, X. Fan, *Adv. Energy Mater.* 2026, **16**, e04549.

[S13] X. Dan, X. Yin, J. Ba, J. Li, Y. Cheng, F. Duan, Y. Wei, Y. Wang, *Nano Lett.* 2024, **24**, 6881.

[S14] Z. Zhu, Z. Lin, Z. Sun, P. Zhang, C. Li, R. Dong, H. Mi, *Rare Metals* 2022, **41**, 3729.

[S15] C. Kang, J. Park, G. Kim, K. Ko, S. Son, *ACS Appl. Mater. Interfaces* 2023, **15**, 7887.

[S16] X. Han, X. Kong, D. Wang, X. Li, L. Dong, *Chem. Eng. J.* 2023, **477**, 147078.

[S17] J. Jiang, Y. Huang, Z. Fan, Y. Cui, X. Liu, X. Wang, *Chem. Commun.* 2025, **61**, 6190.

[S18] L. Zhang, Y. Li, X. Liu, R. Yang, J. Qiu, J. Xu, B. Lu, J. Rosen, L. Qin, J. Jiang, *Adv. Sci.* 2024, **11**, 2401252.

[S19] Y. Zong, H. Chen, J. Wang, M. Wu, Y. Chen, L. Wang, X. Huang, H. He, X. Ning, Z. Bai, W. Wen, D. Zhu, X. Ren, N. Wang, S. Dou, *Adv. Mater.* 2023, **35**, 2306269.

[S20] K. Lolupiman, C. Yang, P. Woottapanit, W. Sukmas, W. Limphirat, N. Rodthongkum, X.

Zhang, G. He, J. Qin, *Adv. Funct. Mater.* 2025, **35**, e24100.

[S21] J. Liu, Y. Zhou, G. Xing, M. Qi, Z. Tang, O. Terasaki, L. Chen, *Adv. Funct. Mater.* 2024, **34**, 2312636.

[S22] Q. He, J. Bai, Y. Liao, H. Wang, L. Chen, *Chem. Eng. J.* 2024, **485**, 149893.

[S23] K. Hua, Q. Ma, Y. Liu, P. Xiong, R. Wang, L. Yuan, J. Hao, L. Zhang, C. Zhang, *ACS Nano* 2025, **19**, 14249.

[S24] T. Song, Q. Ma, B. Wang, X. Zhang, Y. Wang, H. Xiong, *Angew. Chem. Int. Edit.* 2025, **64**, e202503655.

[S25] Y. Ding, C. Cai, L. Ma, J. Wang, M. Mercer, J. Liu, D. Kramer, X. Yu, D. Xue, C. Zhi, C. Peng, *Adv. Energy Mater.* 2025, **15**, 2402819.

[S26] S. Yao, Y. Sun, L. Pan, *Appl. Surf. Sci.* 2024, **672**, 160785.

[S27] H. Shuai, R. Liu, W. Li, X. Yang, H. Lu, Y. Gao a, J. Xu, K. Huang, *J. Colloid Interf. Sci.* 2023, **639**, 292.

[S28] A. Zhang, X. Yin, X. Zhang, J. Ba, J. Li, Y. Wei, Y. Wang, *ACS Appl. Energy Mater.* 2024, **7**, 1298.